Biophysical Chemistry 214–215 (2016) 1–10

Contents lists available at ScienceDirect

Biophysical Chemistry

journal homepage: http://www.elsevier.com/locate/biophyschem

Tensile mechanical properties of collagen type I and its enzymatic crosslinks

Albert L. Kwansa [a,b,*], Raffaella De Vita [b], Joseph W. Freeman [a,c,**]

[a] Virginia Tech-Wake Forest School of Biomedical Engineering and Sciences, Virginia Polytechnic Institute and State University (Virginia Tech), Blacksburg, VA 24061, USA
[b] Department of Biomedical Engineering and Mechanics, Virginia Polytechnic Institute and State University (Virginia Tech), Blacksburg, VA 24061, USA
[c] Department of Biomedical Engineering, Rutgers University, Piscataway, NJ 08854, USA

HIGHLIGHTS

- Constructed collagen type I molecular models with four enzymatic crosslink types
- Employed steered MD to predict stress-strain responses and elastic moduli
- Predicted crosslink (immature vs mature) and position (N vs C terminus) differences
- Used bond dissociation energies to predict differences in crosslink failure modes

GRAPHICAL ABSTRACT

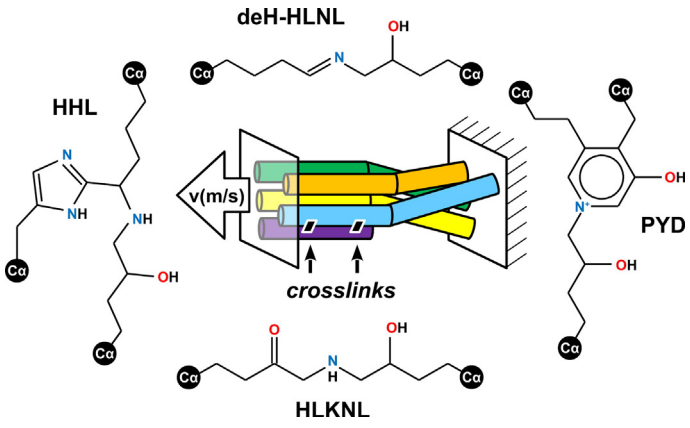

ARTICLE INFO

Article history:
Received 21 January 2016
Received in revised form 14 April 2016
Accepted 17 April 2016
Available online 19 April 2016

Keywords:
Type I collagen
Microfibril
Enzyme-derived crosslink
Molecular dynamics

ABSTRACT

Collagen type I crosslink type and prevalence can be influenced by age, tissue type, and health; however, the role that crosslink chemical structure plays in mechanical behavior is not clear. Molecular dynamics simulations of ~65-nm-long microfibril units were used to predict how difunctional (deH-HLNL and HLKNL) and trifunctional (HHL and PYD) crosslinks respond to mechanical deformation. Low- and high-strain stress-strain regions were observed, corresponding to crosslink alignment. The high-strain elastic moduli were 37.7, 37.9, 39.9, and 42.4 GPa for the HLKNL, deH-HLNL, HHL, and PYD-crosslinked models, respectively. Bond dissociation analysis suggests that PYD is more brittle than HHL, with deH-HLNL and HLKNL being similarly ductile. These results agree with the tissues in which these crosslinks are found (e.g., deH-HLNL/HLKNL in developing tissues, HHL in mature skin, and PYD in mature bone). Chemical structure-function relationships identified for these crosslinks can aid the development of larger-scale models of collagenous tissues and materials.

* Correspondence to: A. L. Kwansa, Present affiliation: Department of Materials Science and Engineering, North Carolina State University, Raleigh, NC 27695, USA.
** Correspondence to: J. W. Freeman, Department of Biomedical Engineering, Rutgers University, 317 BME Building, 599 Taylor Rd., Piscataway, NJ 08854, USA.
E-mail addresses: alkwansa@vt.edu (A.L. Kwansa), joseph.freeman@rutgers.edu (J.W. Freeman).

http://dx.doi.org/10.1016/j.bpc.2016.04.001
0301-4622/

1. Introduction

Collagens are a family of extracellular matrix (ECM) proteins that comprise both vertebrate and invertebrate tissues [1,2]. In mammals, collagens are especially abundant, comprising up to one-third of total body protein by weight [3–5]. There are ~27 types of collagens that have been identified; they are often classified as fibril-forming, network-forming, and fibril-associated collagens [6]. Type I collagen is the most prevalent; it is a fibril-forming collagen found in connective tissues such as tendon, ligament, bone, skin, and the cornea of the eyes [6,7], where it functions to provide tensile strength and to serve as a biological scaffold for cells and other ECM components [8]. The strength of type I collagen and other fibril-forming collagens has been attributed to their molecular structure (300 × 1.5-nm triple helix), their assembly into supramolecular structures (microfibrils, subfibrils, and fibrils), and their chemical crosslinks (covalent bonds formed between amino acid side chains).

Collagen crosslinks include enzymatic crosslinks that form in early development and throughout maturation, and non-enzymatic crosslinks that are more prevalent in old age or in certain disease states (e.g., diabetes) [9]. Enzymatic crosslinks form initially as immature, difunctional crosslinks that connect only two amino acids. Over time, these immature crosslinks can react further to form mature, trifunctional crosslinks that connect three amino acids [10]. Immature, difunctional crosslinks include aldimines and ketoimines, while mature, trifunctional crosslinks include pyridinolines, pyrroles, and histidine-derived crosslinks [10–12] (Fig. 1). The prevalence of different collagen crosslinks normally changes with age and varies between different connective tissues [13,14]. However, certain rare connective tissue disorders involve improper crosslinking, most often due to genetic mutations that directly or indirectly affect enzymes involved in crosslink formation [13,15,16]. These disorders can lead to fragile skin and eyes (Ehlers–Danlos syndrome type 6A), brittle bones and stiff joints (Bruck syndrome type 2), loose and inelastic skin (Cutis laxa type 4), and hardening and lesioning of skin (scleroderma) [13,15,16]. These symptoms describe, in part, alterations to the mechanical behaviors of the affected connective tissues, in which fibril-forming collagens are major load bearing units. Thus, investigations of the mechanical properties of fibril-forming collagens can contribute to an improved understanding of mechanical dysfunctions of these tissues as well as the mechanical performance of collagenous materials used more broadly.

Within the last ~10 years, techniques and technologies have been developed to mechanically characterize and model fibril-forming collagens at smaller scales. Such collagens have been characterized and modeled at the molecular level (e.g., optical tweezers [17,18], atomic force microscopy (AFM) [19], and molecular dynamics (MD) [20]); modeled at the microfibril level (e.g., MD [21] and

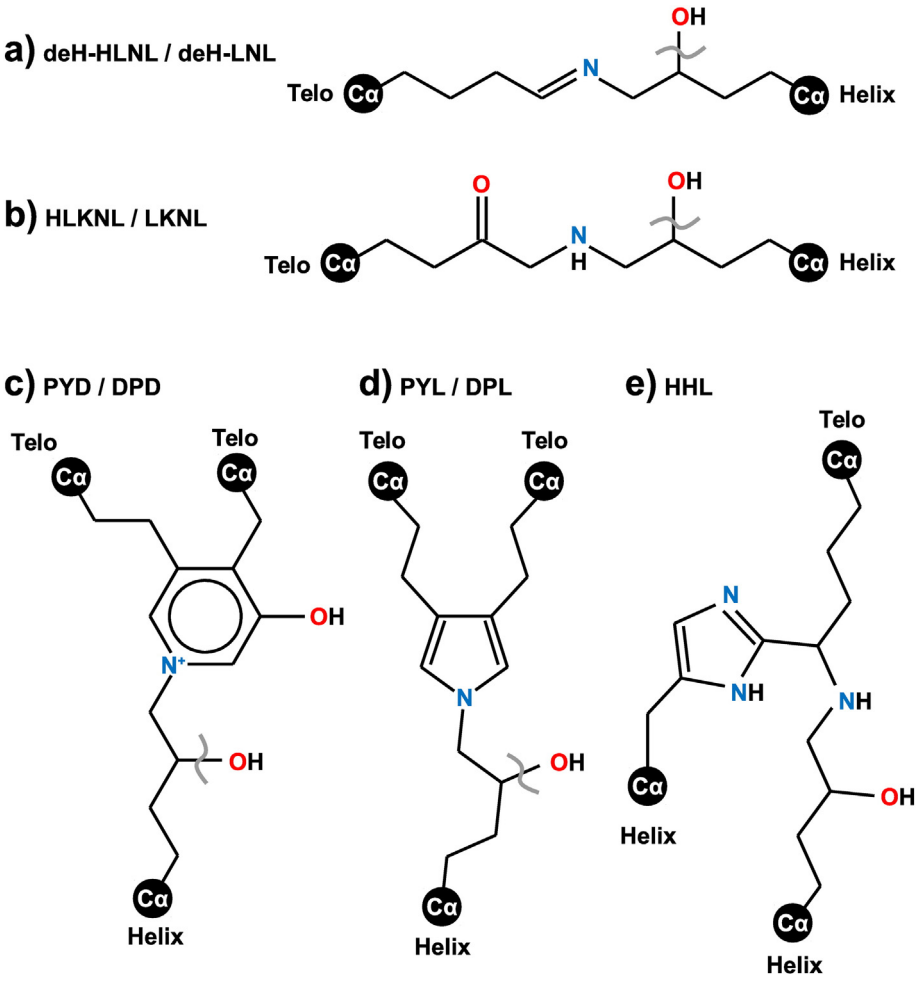

Fig. 1. Chemical structures of nine different enzymatic collagen crosslinks. (Subfigures a-d are intended to show two crosslinks with one drawn structure, with the difference being the presence or absence of a hydroxyl group denoted by a curved gray line. For each pair of crosslinks listed below, the first crosslink possesses this hydroxyl group, while the second crosslink lacks this hydroxyl group.) Immature, difunctional crosslinks include (a) aldimines (dehydro-hydroxylysino-norleucine (deH-HLNL) and dehydro-lysino-norleucine (deH-LNL)) and (b) ketoimines (hydroxylysino-keto-norleucine (HLKNL) and lysino-keto-norleucine (LKNL)). Mature, trifunctional crosslinks include (c) pyridinolines (hydroxylysyl pyridinoline (PYD) and lysyl pyridinoline (DPD)), (d) pyrroles (hydroxylysyl pyrrole (PYL) and lysyl pyrrole (DPL)), and (e) histidinyl hydroxylysino-norleucine (HHL).“Helix” and “Telo” indicate whether the precursor amino acid was from the triple-helical domain or one of the telopeptide domains, respectively. These drawings were generated using ACD/ChemSketch [74], based on structures depicted by Bailey et al. [75].

finite-element models [22]); and characterized and modeled at the fibril level (e.g., AFM [23–25], microelectromechanical systems (MEMS) [26–28], Kelvin–Voigt-based models [29], and mesoscopic models [30]). However, models of crosslinked collagens have, thus far, treated the enzymatic crosslinks generally without distinguishing between different enzymatic crosslink types.

Herein, we describe the use of molecular dynamics to model collagen type I at the microfibril level while accounting for four different enzymatic crosslink types, namely, dehydro-hydroxylysino-norleucine (deH-HLNL), hydroxylysino-keto-norleucine (HLKNL), histidinyl hydroxylysino-norleucine (HHL), and hydroxylysyl pyridinoline (PYD) (Fig. 1). In particular, we have modeled the response of microfibril units (i.e., a ~65-nm-long portion of a microfibril) and their crosslinks to uniaxial tensile deformation. A preliminary application of this MD simulation data to predict the mechanical behavior of collagen fibrils is also briefly discussed.

2. Materials and methods

2.1. Computer hardware

All molecular dynamics simulations were conducted using (1) a 34-node Linux computing cluster operated by Virginia Tech's Engineering Science and Mechanics Department, (2) a 1024-node Mac OS X/Linux computing cluster called "System X" from Virginia Tech's Advanced Research Computing unit, and (3) a 42-node Linux computing cluster called "Athena" from Virginia Tech's Advanced Research Computing unit.

2.2. Computer software and force field

Our molecular models were constructed using Discovery Studio Visualizer (DS Visualizer) [31] and Visual Molecular Dynamics (VMD) [32]. All molecular dynamics simulations were carried out using the Nanoscale Molecular Dynamics (NAMD) code [33], and the Tachyon ray tracing code was used with VMD to generate representative images from the simulation trajectory files [34]. The CHARMm 22 parameter file (PARM.PRM) and topology file (AMINO_NA.RTF) from DS Visualizer were used with the NAMD code, after receiving permission from Accelrys Software, Inc. [31]. Partial charges for the crosslinks (i.e., crosslinked amino acid residues) were assigned via the Momany-Rone partial charge method, using DS Visualizer [31,35]. Topology file entries for the crosslinks (deH-HLNL, HLKNL, HHL, and PYD) were manually added as residue patches to the end of the topology file; each crosslink was assigned a formal charge of "0.00" except for PYD, which was given a formal charge of "1.00" (see Fig. 1 for the chemical structures of these crosslinks).

2.3. Construction of the collagen type I microfibril units

The triple-helical structure was based upon the coordinates of a 29-amino acid-long collagen-like (proline-proline-glycine)$_n$ crystal

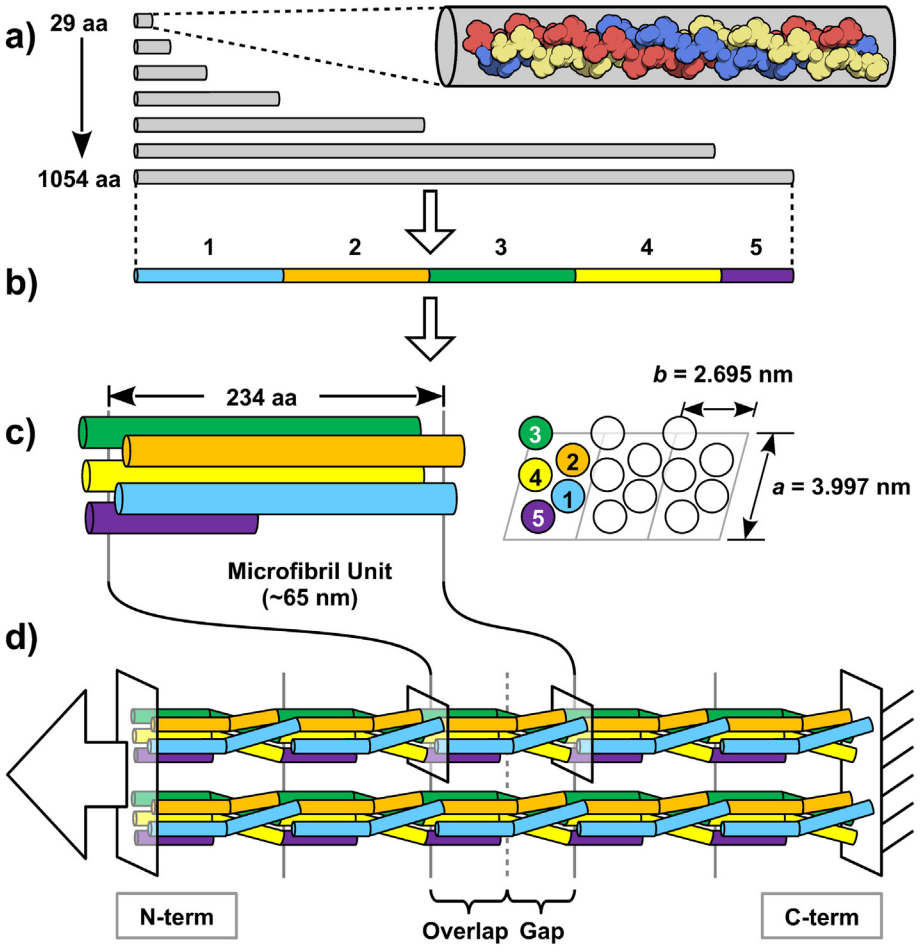

Fig. 2. A schematic of steps used to assemble the microfibril unit models: (a) lengthening of a short collagen-like X-ray structure (1k6f.pdb) from a length of 29 amino acids (29 aa) to 1054 amino acids (1054 aa), (b) division into five molecular segments, and (c) axial and lateral translations of the five segments to form a microfibril unit with a length of 234 amino acids (234 aa) [38,40]. The molecular image in (a) is of the 1k6f.pdb X-ray structure [36]; this molecular image was generated using the computer program QuteMol [76]. (d) Curved lines leading to a microfibril unit after applying molecular kinks within the gap region. This microfibril unit is shown with nine additional copies or images of itself to provide a simplified visualization of how we envisioned a modeled microfibril unit would appear in the context of a fibrillar structure.

structure; these coordinates were acquired from the RCSB Protein Data Bank (PDB ID: 1K6F) [36]. Using DS Visualizer, crystallographic water molecules were removed, and the structure was replicated and spliced together, similar to methods described by Chen et al. [37], to form a single collagen-like molecule containing 1054 amino acids per chain (Fig. 2a). This collagen-like molecule was then divided into five molecular segments (Fig. 2b), which were subsequently aligned at their N-termini and translated into specific x–y coordinates to represent a quasi-hexagonal compressed microfibril unit (Fig. 2c) [38]. This microfibril unit effectively contained one collagen type I molecule (i.e., one-fifth the size of a complete microfibril).

Then using VMD, molecular kinks (i.e., changes in the tilt angle of the long axis of the triple helix relative to the long axis of the microfibril) were applied, within the gap region only, in order to establish a microfibrillar twist [39,40]. Tilt angles were calculated for each of the four longer segments (Fig. 2c: segments 1 to 4) so that the segments could be tilted at the start of the gap region towards the position of the next segment as shown in Fig. 2d (e.g., within the gap region, segment 1 begins at position #1 and ends at position #2); the tilt angles ranged from 2.23 to 2.86 degrees. Then one of the three chains was trimmed from 1054 to 1021 amino acids leading to an α1-α2-α1 collagen-like microfibril unit. Thus, the model contained an N-telopeptide domain (16 amino acids for α1 and 6 for α2), a triple-helical domain (1014 for α1 and α2), and a C-telopeptide domain (24 for α1 and 1 for α2). The conformations of the N- and C-telopeptides were then adjusted based upon a rat tail tendon collagen type I X-ray fiber diffraction structure (PDB ID: 3HR2) [41], allowing for favorable alignments between four potential crosslinking sites (i.e., two pairs of crosslinking sites) [13,42–44]. Bovine (*Bos taurus*) collagen type I amino acid sequences for the 1054-residue-long α1 chains and the 1021-residue-long α2 chain were then used to replace the collagen-like Pro-Pro-Gly sequences [41,45,46]; these bovine sequences included hydroxylysines and hydroxyprolines. The following UniProt accession numbers were used: P02453 (collagen type I α1) and P02465 (collagen type I α2).

Four crosslinked models were then derived from the uncrosslinked model by applying patches (entries added to the CHARMM topology file for the crosslinks to join their amino acid precursors) during the generation of CHARMM PSF structure files for each model. Rendered snapshots of the uncrosslinked model and four crosslinked models are shown in Fig. 3a.

2.4. Energy minimization, heating, and equilibration

Energy minimization via the conjugate gradients method was performed until a NAMD gradient tolerance of 0.1 kcal/mol/nm. For heating, temperature reassignment was used to increase the temperature from 0 to 293.15 K over 10 ps. During subsequent equilibration steps, the Langevin dynamics method (langevinDamping $= 5\ ps^{-1}$) was used for temperature control at 293.15 K. The generalized Born implicit solvent (GBIS) approach of Onufriev, Bashford, and Case (GB^{OBC} II) was used to indirectly model the effects of solvent and ions [47]. The solvent dielectric, ion concentration, and GBIS alpha cutoff were set to 80.0, 0.150 mol/L, and 1.4 nm, respectively. The simulation timestep was initially 1 fs during energy minimization, heating, and the initial stages of equilibration; it was later switched to 2 fs during the remaining equilibration time. Non-bonded interactions were treated with a switching distance of 1.5 nm, a cutoff of 1.6 nm, and a pair list distance of 1.75 nm. The solvent dielectric of 80.0 was selected in representation of water at 293.15 K and 1 atm, and the ion concentration of 0.150 mol/L was selected to match physiological saline solution (i.e., 0.9% g/mL sodium chloride in water). The non-bonded distances (1.5–1.6–1.75 nm) and the GBIS alpha cutoff (1.4 nm) were based upon values recommended for GBIS in the NAMD 2.8 user's guide [48].

2.5. Constant velocity pulling

In order to conduct constant velocity pulling simulations with the microfibril units, C-terminal Cα atoms from four segments were fixed, and N-terminal Cα atoms from four segments were pulled in the N-terminal direction at a constant velocity using NAMD's "moving constraints" feature (Fig. 3b). A spring constant of 9999.00 kcal/mol/$Å^2$ was used for all pulled atoms [49]. The purpose of the fixed and pulled atoms was to mimic the continuity of the collagen molecules beyond a single microfibril unit and the presence or absence of crosslinks tethered

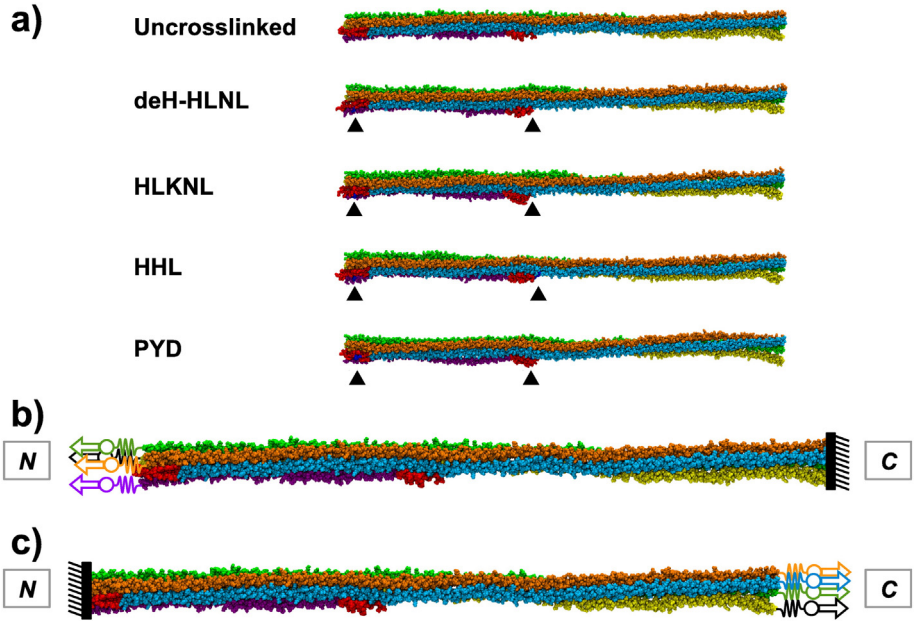

Fig. 3. (a) Rendered snapshots of the uncrosslinked and crosslinked molecular models. (b and c) Representative schematics of the constant velocity pulling simulations superimposed on rendered snapshots of the molecular models. In (b), 12 C-terminal Cα atoms are fixed (thick line with hash lines) and 12 N-terminal Cα atoms are pulled in the N-terminal direction; each pulled Cα atom is connected through a virtual spring of stiffness *k* to a virtual atom (open circle) that moves at a constant velocity *v*. In (c), the constant velocity pulling is in the opposite direction relative to (b) including a switching of the fixed and pulled ends of the model (i.e., 12 N-terminal Cα atoms are fixed and 12 C-terminal Cα atoms are pulled in the C-terminal direction). In (a–c), the color scheme is identical to that described in Fig. 2 with the addition of red for the N- and C-terminal telopeptides and dark blue for the crosslinks; the positions of the crosslinks are indicated by filled triangles. All snapshots were rendered with VMD [32] and Tachyon [34].

to the ends of the molecules. Segment 1 was not pulled since the molecule of which it is a part has no continuity into the next microfibril unit in the N-terminal direction. Similarly, segment 5 was not fixed since the molecule of which it is a part has no continuity into the next microfibril unit in the C-terminal direction (see Fig. 2c for the segment number references and Fig. 2d for a schematic of the described continuity). It was assumed, for simplicity, that for the crosslinked or uncrosslinked microfibril units, all microfibril units in the longitudinal direction were identically crosslinked or uncrosslinked, respectively. Therefore, 12 fixed and 12 pulled Cα atoms were used for all crosslinked models (deH-HLNL, HLKNL, HHL, and PYD), while 3 fixed and 12 pulled Cα atoms were used for the uncrosslinked model. Multiple pulling velocities (100, 50, 25, 12.5, and 6.25 m/s) were used to identify any rate dependence. In order to assess the influence of the pulling direction, an additional simulation was conducted with the deH-HLNL-crosslinked model during which the N-terminal end was fixed and C-terminal end pulled in the C-terminal direction (Fig. 3c). Each pulling simulation was conducted three times ($n = 3$).

2.6. Microfibril unit analysis: engineering strain, strain energy, cross-sectional area, and nominal stress

Engineering strains of the microfibril units were calculated from changes in length of the microfibril units divided by their initial lengths. Each initial length was calculated as the root-mean-squared (RMS) distance between the fixed and pulled atoms, and changes in length were calculated as the RMS displacement of the pulled atoms over time. These RMS calculations were performed using the RMSD Trajectory Tool within VMD [32]. Strain energy was computed as the change in total energy relative to the initial unstrained state.

Initial cross-sectional areas of the microfibril units were obtained using a protein data bank (PDB) analysis package called PDBAN, which was written by the laboratory of Prof. Sergei Sukharev at the University of Maryland [50], using MATLAB® [51]. Volumetric data files were generated using a probe radius of 0.14 nm, van der Waals radii from the CHARMm 22 all-atom force field, and a resolution of 0.1 nm. Initial cross-sectional areas were then calculated, normal to the long-axis of the microfibril units, in 0.1-nm increments along the length of each microfibril unit and averaged to obtain a single cross-sectional area value per model.

Forces and nominal stresses (σ) were derived from strain energy (W) vs. extension (ΔL) data, which were each fitted with a 6th order polynomial function: $W(\Delta L) = \sum C_n * \Delta L^n$, where $n = 2$ to 6. These strain energy functions were used to derive nominal stress functions by taking the first derivative of strain energy with respect to extension and dividing by the initial cross-sectional area (A_0) and Avogadro's number (N_A): $\sigma(\Delta L) = \sum (n * C_n * \Delta L^{n-1}) / (A_0 * N_A)$. The following two conditions were imposed: $W(0) = 0$ and $\sigma(0) = 0$. In order to satisfy these two conditions, the coefficients C_0 and C_1 were set to zero. The remaining five coefficients C_2 to C_6 were determined via Microsoft Excel using its LINEST function, in an array formula, for non-linear least-squares fitting.

Due to the low- and high-sloping regions of the nominal stress data, two elastic moduli were calculated, namely, a low-strain modulus and a high-strain modulus. The distinction between the low- and high-strain regions was made based on the determination of a transition point, which was defined as the extension value at which the second derivative of the nominal stress function was maximal (i.e., the extension value at which the third derivative of the nominal stress function was zero).

2.7. Crosslink analysis: strain energy, alignment, and strain

Crosslink strain energy was calculated as the change in total energy as computed by the NAMD code [33]. This total energy was calculated only for atoms in between the alpha carbon (Cα) atoms of the crosslinks (i.e., excluding other backbone atoms). Crosslink alignment was defined as the orientation angle of the crosslinks relative to the long axis of the microfibril unit model (90° = perpendicular alignment; 0° = parallel alignment). Orientation angles were calculated as $\theta = 90 - \tan^{-1}[|Z_2 - Z_1| / \mathrm{SQRT}((X_2 - X_1)^2 + (Y_2 - Y_1)^2)]$, where X_1, Y_1, Z_1 and X_2, Y_2, Z_2 represent the x, y, and z coordinates of two Cα atoms. In all cases, angle calculations were done between a "Telo" (telopeptide) and "Helix" (triple helix) Cα pair (see Fig. 1). This calculation was straightforward for deH-HLNL and HLKNL, since these crosslinks contain only one Cα pair each; however, for HHL and PYD, two Telo-Helix angles were calculated and averaged. Crosslink strain was calculated as the change in distance between pairs of Cα atoms divided by the initial distance. Similar to crosslink alignment, strain of the HHL and PYD crosslinks was based on an averaging of results from two Cα pairs.

2.8. Statistical analysis

Statistical analysis was used to compare the elastic moduli of the microfibril units. All statistical analysis was performed using the JMP statistical software [52]. Unless otherwise stated, the significance level (alpha value) was set to 0.05. A Welch's one-way ANOVA and Student's t-tests with Bonferroni correction were used. For the Bonferroni correction, the alpha value was set to 0.05 divided by the number of t-tests, where the number of t-tests was calculated as $g * (g - 1) / 2$ with g being the number of compared groups.

3. Results and discussion

3.1. Pulling velocity

Five pulling velocities were employed for the present work, namely, 100, 50, 25, 12.5, and 6.25 m/s. These velocities are several orders of magnitude faster than those utilized during the experimental mechanical characterization of collagen fibers ($3.3 * 10^{-4}$ to $3.3 * 10^{-5}$ m/s [53]) and collagen fibrils ($4.6 * 10^{-6}$ m/s [54], $7.4 * 10^{-7}$ m/s [24], and $3.4 * 10^{-8}$ m/s [27]). The use of accelerated pulling simulations, relative to experiments, is currently necessary due to the computational resources and time that would be needed to access experimental velocities. For example, our simulations involved up to ~10 ns of simulation time with a simulation performance of ~2 ns/day (64 CPU cores) leading to a real-world time of up to ~5 days per simulation and a cumulative real-world simulation time of up to ~75 days (when considering 5 crosslink states and 3 repetitions per simulation).

Our pulling velocities are, however, similar to those that have been used for steered molecular dynamics-based investigations of the mechanical functions of various proteins. As others have noted, the accelerated simulation velocities, while providing useful insights, should be interpreted appropriately. For instance, Lu et al. employed 100 and 50-m/s SMD for the muscle protein titin and reported forces that were four times higher than 50-m/s-extrapolated experimental forces; their reasoning was that the forced unfolding and accelerated simulation pulling rates led to a dominance over energetic barriers to unfolding and the application of irreversible work [55]. Gao et al. utilized 5 and 1-m/s SMD to study unfolding of the extracellular matrix protein fibronectin type III; they reported simulation rupture forces that were an order of magnitude higher than those from AFM experiments [56]. With a broad range of SMD pulling velocities (100 to 0.01 m/s), Gautieri et al. reported that the elastic moduli of a 30-residue-long collagen-like molecule pulled in uniaxial tension exhibited rate independence with velocities of <0.5 m/s; velocities above 0.5 m/s led to elevated elastic moduli and differences in triple-helical unfolding dynamics [57]. In our previous work, we employed 100 to 1.5625 m/s to shear two collagen type I molecular segments chemically crosslinked with two deH-HLNL crosslinks (an N-terminal crosslink and a C-terminal crosslink); we reported negligible differences between 6.25, 3.125, and 1.5625 m/s, based on strain energy responses of the crosslinked molecular segments and of the individual N- and C-crosslinks [49]. Based on the results from

our earlier work, we chose to use 6.25 m/s as our slowest pulling velocity in the present work. However, we acknowledge that the results presented in the subsequent sections are likely in some overestimation of what might be obtained if experimentally relevant velocities were utilized. In the following sections, we have also assumed that the relative differences and trends identified for the uncrosslinked and different crosslinked models at the velocities investigated are valid for more experimentally relevant velocities.

3.2. Microfibril units: engineering strain, strain energy, and nominal stress

The initial lengths of the five microfibril unit models (L_0) averaged 64.61 ± 0.10 nm, while their initial cross-sectional areas (A_0) averaged 7.57 ± 0.02 nm^2. These ~65-nm initial lengths are slightly shorter than the ~67-nm length that is typically reported for the D-period of tendon collagen fibrils (e.g., 67.79 nm for rat tail tendon [41]). However, it has been reported, based on small-angle X-ray scattering (SAXS), that rat tail tendon collagen fibrils can exhibit a 2.5% reduction in D-periodicity (e.g., 67 nm to 65 nm) when dehydrated from 95% relative humidity (RH) to 5% RH [58]. Thus, one reason for our ~65-nm lengths may have been our use of implicit solvent rather than explicit solvent. The lack of explicit water, structural or closely bound water in particular, likely contributed to the reduced D-periodic lengths of our models [59].

Mechanical responses of the microfibril unit models are shown in Fig. 4a (strain energy-extension) and Fig. 4b (nominal stress-engineering strain) for the 6.25 m/s extension rate; the data sets are similar at lower extensions and strains but are more distinguishable at higher extensions and strains. The mature PYD-crosslinked model exhibited the greatest levels of strain energy and nominal stress, followed by the mature HHL-crosslinked model, the immature (deH-HLNL and HLKNL)-crosslinked models, and the uncrosslinked model. The mechanical responses of the models are non-linear, which may be attributed to the straightening of triple-helical conformations [29] and alignment of the N- and C-terminal crosslinks [49]. This non-linear behavior includes a low-strain region and high-strain region; the low-to-high strain transition region for the crosslinked models was calculated as 26.72 ± 0.16% strain (Fig. 4b). The strain-energy response of the uncrosslinked model also displays a transition, described by an increase to a maximum and a decrease thereafter (inset of Fig. 4a), which is likely due to the onset of intermolecular shearing.

3.3. Elastic moduli

Low- and high-strain elastic moduli for the microfibril units pulled at 6.25 m/s are shown in Fig. 5. The low-strain modulus of the crosslinked models was insensitive to the crosslink type; however, the high-strain modulus was significantly affected. Of the crosslinked models, the models containing the immature crosslinks (HLKNL and deH-HLNL) led to the lowest high-strain elastic moduli (37.7 ± 0.23 and 37.9 ± 0.31 GPa, respectively), followed by the HHL-crosslinked model (39.9 ± 0.29 GPa), and then by the PYD-crosslinked model (42.4 ± 0.21 GPa). It was also found that the pulling direction had no significant influence over the low- or high-strain moduli. Regarding the pulling velocity, it was determined that there was a significant influence for 100, 50, and 25, but not for 12.5 and 6.25 m/s, based on Student's *t*-tests with Bonferroni correction.

3.4. Crosslink alignment, strain, and strain energy

Each of the crosslinked microfibril units contained two crosslinks: one near the N-terminal end (N-crosslink) and another near the C-terminal end (C-crosslink). In all cases, the N-crosslinks aligned more readily (Fig. 4c), were strained sooner (Fig. 4d), and exhibited greater levels of strain energy (Fig. 4e) relative to the C-crosslinks. It can be seen that during the low-strain region, the N- and C-crosslinks exhibit negligible strain energy and begin to undergo alignment. However, during the high-

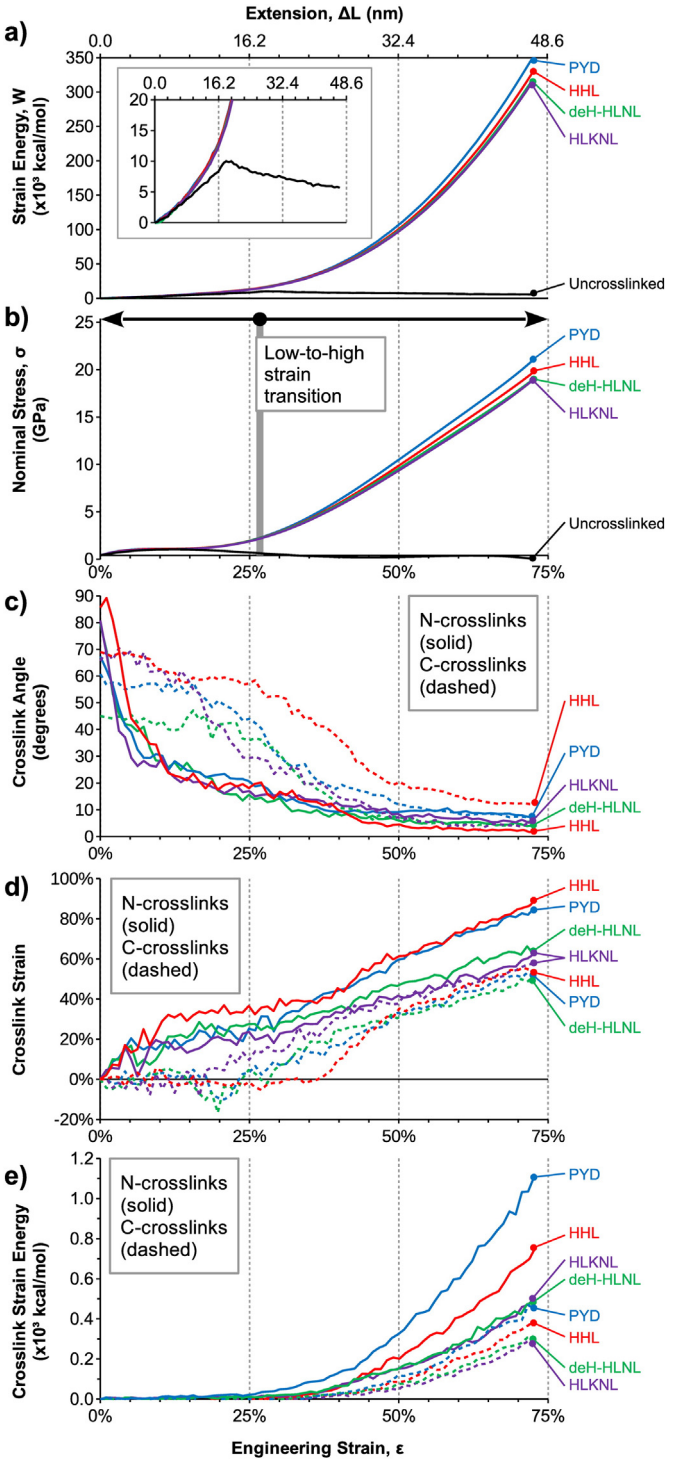

Fig. 4. (a) Strain energy-extension data for the microfibril unit models at 6.25 m/s. Here, strain energy represents the change in total energy as a function of extension. The inset figure provides a closer view of the response of the uncrosslinked model. (b) Stress-strain data for the microfibril unit models at 6.25 m/s. Here, nominal stress was derived from the strain energy data, and engineering strain was derived from the extension data and the initial lengths. The vertical solid line represents the average strain value calculated for the transition between the low- and high-strain regions for the four crosslinked models pulled at 6.25 m/s (26.72 ± 0.16% strain). (c) Crosslink orientation angles for the immature and mature crosslinks at 6.25 m/s, measured relative to the long axis of the microfibril unit models. (d) Crosslink strain of the immature and mature crosslinks at 6.25 m/s. (e) Strain energy in the immature and mature crosslinks at 6.25 m/s. For (c–e), solid lines denote the N-terminal crosslinks, and dashed lines denote the C-terminal crosslinks.

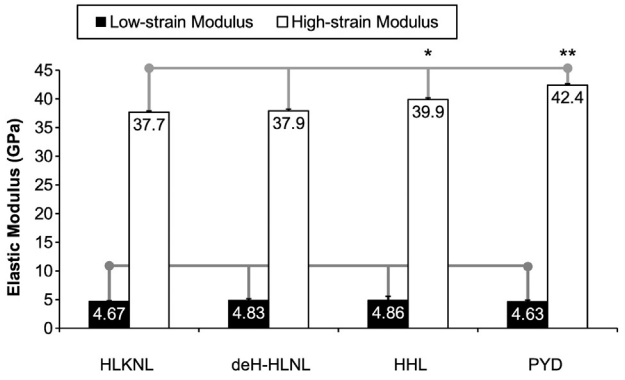

Fig. 5. Low- and high-strain elastic moduli for the microfibril unit models at 6.25 m/s. The plotted values each represent a mean + standard deviation ($n = 3$). Statistical analyses (Welch's one-way ANOVA with alpha = 0.05 and Student's *t*-tests with a Bonferroni-corrected alpha = 0.0083 = 0.05/(g ∗ (g − 1) / 2), where g = 4 groups) were conducted separately for the low- and high-strain moduli. The gray lines connecting the plotted bars denote the groups being compared, and the asterisks denote statistical significance from the Student's *t*-tests ($p < 0.0083$).

strain region, the N- and C-crosslinks continue to align, exhibit a near-linear increase in strain, and display a non-linear increase in strain energy (Fig. 4c–e). These differences in the N- and C-crosslinks are consistent with that reported in our earlier work [49], suggesting that the crosslink mechanical recruitment mechanism proposed for the deH-HLNL crosslink [49] is applicable to other immature and mature crosslinks. The mature PYD crosslink displayed the greatest levels of strain energy, followed by the HHL crosslink, and then by the immature crosslinks (deH-HLNL and HLKNL). This order is consistent with that observed for the strain energy, nominal stress, and high-strain elastic moduli data reported for the microfibril unit models (Figs. 4 and 5).

These results can be attributed to the chemical structures of these crosslinks. The two immature, difunctional crosslinks (deH-HLNL and HLKNL) are structurally very similar. Both possess 10 load-bearing bonds all arranged in series between their alpha carbon atoms (Fig. 1). The only difference is one of these 10 bonds (a C—N single bond for HLKNL and a C—N double bond for deH-HLNL); this C—N double bond was modeled with a slightly higher bond stretching force constant relative to this C—N single bond (Fig. 6a–b) [31,60]. Therefore, the effective stiffness of deH-HLNL would be expected to be slightly higher than HLKNL, which explains why the low- and high-strain moduli of the deH-HLNL-crosslinked microfibril unit were marginally greater than those of the microfibril unit with HLKNL (Fig. 5). The two mature, trifunctional crosslinks (HHL and PYD), however, are more complex. PYD consists of a six-membered, aromatic ring structure from which its three crosslinked amino acids emanate. This aromatic ring contains six partial double bonds which, from a molecular mechanics stand point, are stiffer than single bonds (Fig. 6c). In contrast, HHL consists of three crosslinked amino acids that emanate from an aliphatic/non-aromatic carbon (i.e., three single bonds); two of these three amino acids contribute a linear series of single bonds, while the third amino acid contributes an aromatic, five-membered ring structure (Fig. 6d). Thus, the underlying molecular mechanics approach would lead one to hypothesize that the trifunctional structure and aromaticity of HHL and PYD afford an increased effective stiffness, which was confirmed by the molecular dynamics simulations (Figs. 4e and 5). That is to say, the trifunctional structure of these mature crosslinks provided them with an increased stiffness relative to the difunctional, immature crosslinks, and the specific aromatic structures of HHL and PYD afforded them each with a unique stiffness.

3.5. Bond stretching and crosslink failure

The CHARMm 22 all-atom force field, employed for this MD study, utilizes a quadratic function to model bond stretching energy, namely, $K_b(b - b_0)^2$, where K_b is the force constant [kcal/mol/Å^2], b is the current bond length [Å], and b_0 is the equilibrium bond length [Å] [31,60]. Quadratic bond stretching functions are characteristic of the AMBER, CHARMM/m, GROMOS, OPLS, and TRIPOS force fields (Table 2.4 in reference [61]). Such quadratic functions closely match results from quantum mechanics calculations when b is close to b_0; however, marked deviations from b_0 lead to an overestimation of bond stretching energy (Fig. 2.2 in reference [61]). A more accurate, although more computationally expensive, approximation for bond stretching energy is achievable via the Morse Potential [62], e.g., $D_e(1 - \exp[-\alpha(b - b_0)])^2$, where D_e is the bond dissociation energy [kcal/mol] and α is a fitting parameter [1/Å] [61]. The Morse Potential is implemented in certain force fields (e.g., CVFF, DREIDING, and UFF); however, such force fields are designed to cover a broader range of molecules and are typically not optimized for the modeling of specific classes of molecules (e.g., proteins) (Table 2.4 in reference [61]). For this reason, a quadratic bond stretching force field, namely, CHARMm, was employed for the present work.

Given the use of a quadratic bond stretching force field with a system undergoing deformation, we sought to follow up with an analysis of how the crosslinks might be expected to fail. Bond dissociation energies for the bonds of the immature and mature crosslinks were assigned based on similar chemical configurations found in Table 4.11 of reference [63]; the assigned bond dissociation energies are included in Fig. 6. The weakest of these bonds is the carbon-nitrogen single bond (D_e = 79.11 kcal/mol based on $H_3C–NH_2$), followed by the carbon–carbon single bond (D_e = 87.95 kcal/mol based on $H_3C–CH_3$), carbon-nitrogen partial double bond (D_e = 116.52 kcal/mol), carbon–carbon partial double bond (D_e = 125.48 kcal/mol), carbon-nitrogen double bond (D_e = 153.92 kcal/mol based on $H_2C=NH$), and carbon–carbon double bond (D_e = 163.00 kcal/mol based on $H_2C=CH_2$) [63].

In Fig. 6, the predicted sites of initial covalent bond failure are marked with filled triangles, and large arrows are used to denote the directions in which the crosslinks were deformed during the MD simulations. For deH-HLNL, HLKNL, and PYD, a C—N single bond is denoted as a predicted site of failure (Fig. 6a–c). However, for HHL, the series of C—C single bonds connected to the telopeptide domain are marked as potential sites of failure, because this branch of the crosslink is not sharing load with another branch (i.e., one branch is attached to the telopeptide domain and two branches are attached to triple-helical domain) (Fig. 6d). Thus, HHL and PYD are predicted to fail at a C—C single bond (D_e = 87.95 kcal/mol) and C—N single bond (D_e = 79.11 kcal/mol; K_b = ~1.5× stiffer than C—C single), respectively. Given that HHL's failure sites are predicted to be more compliant and stronger than that of PYD, PYD is expected to behave in a more brittle manner relative to HHL. The differences reported and discussed for crosslink stiffness and strength are interesting given that deH-HLNL and HLKNL are found in younger and/or healing tissues; PYD crosslinks in stiffer and less ductile connective tissues such as mature bone, tendon, and ligament; and HHL in more compliant and more ductile tissues such as mature skin and cornea [10,14,64–71].

3.6. Preliminary application

An early application of this MD-predicted microfibril-level stress-strain data has been conducted. Specifically, we have used the stress-strain data reported herein (Fig. 4b) to predict the stress-strain response at the level of a hydrated collagen fibril. This fibril-level stress-strain data was then used to predict elastic moduli with different levels of crosslinking. Details on the methods employed for these fibril-level predictions can be found in reference [72]. Fig. 7 shows our predictions of low- and high-strain elastic moduli of a hydrated bovine collagen type I fibril with 1 or 2 mol of crosslink per collagen molecule; the contribution of the crosslinked data was based on an average of the four crosslinked model data curves. These results were compared with previously published data [23–25,27–30,73]. We observed

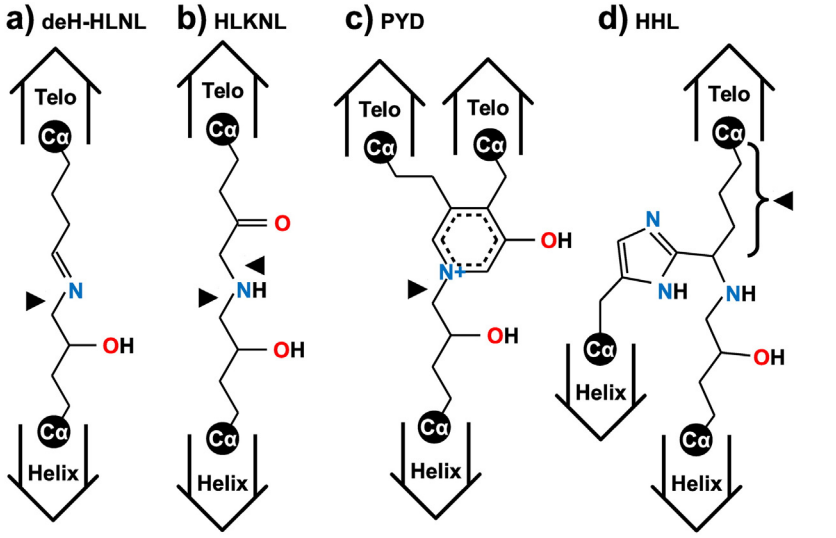

Bond Schematic	Bond (from [63])	Dissociation, kcal/mol (relative to C-C single)	Force Constant relative to C-C single
—— N	$H_3C - NH_2$	79.11 (~0.9x)	~1.2x (both non-aromatic) ~1.5x (aromatic N)
——	$H_3C - CH_3$	87.95 (1.0x)	1.0x (both non-aromatic) ~1.4x (one aromatic C)
------ N	--	116.52 (~1.3x)	~1.6x (both aromatic)
------	--	125.48 (~1.4x)	~1.7x (both aromatic)
═══ N	$H_2C = NH$	153.92 (~1.8x)	~1.4x
═══	$H_2C = CH_2$	163.00 (~1.9x)	~1.8x

Fig. 6. Bond dissociation energies (absolute and relative) and CHARMm 22 force constants (relative) assigned to the bonds of (a) deH-HLNL, (b) HLKNL, (c) PYD, and (d) HHL for the purpose of discussing potential crosslink failure mechanisms. The assigned bond dissociation energies are based on similar chemical configurations found in Table 4.11 of reference [63]; bond dissociation energies for the partial double bonds were calculated as averages of the single- and double-bond values.

very good agreement with two reports based on models ([29,30]) and two experimental reports ([23,73]) but less agreement with other experimental reports ([24,25,27,28]). Additional discussion of model assumptions and simplifications can be found in reference [72].

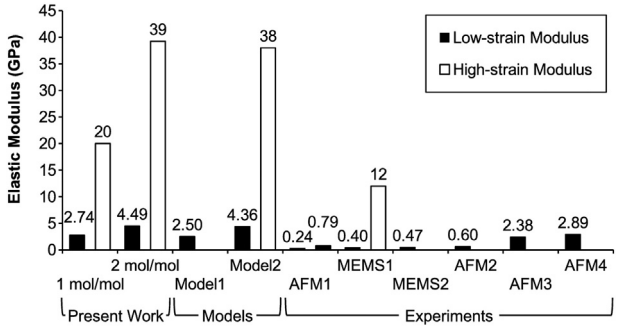

Fig. 7. Low- and/or high-strain elastic moduli for our fibril model plotted with published data. The published model data includes Model1 (a Kelvin–Voigt-based model [29]) and Model2 (a 2-D mesoscopic model [30]). The published experimental data includes AFM1 (AFM testing of bovine Achilles tendon collagen fibrils [24]), MEMS1 (MEMS testing of sea cucumber dermis collagen fibrils [28]), MEMS2 (MEMS testing of sea cucumber dermis collagen fibrils [27]), AFM2 (AFM testing of bovine Achilles tendon collagen fibrils [25]), AFM3 (AFM testing of deer antler bone collagen fibrils [23]), and AFM4 (AFM testing of human patellar tendon collagen fibrils [73]).

4. Summary and conclusions

MD simulations were employed to model ~65-nm-long collagen type I microfibril units. Five microfibril units were assembled, namely, uncrosslinked or crosslinked with two identical crosslinks (immature deH-HLNL, immature HLKNL, mature HHL, or mature PYD). Each microfibril unit was deformed with uniaxial tension at a constant velocity by fixing and pulling specific alpha carbon atoms at the N- and C-termini. The different crosslink types led to significant increases in the high-strain elastic moduli, but not the low-strain moduli. The mature PYD crosslink led to the highest elastic moduli (42.4 ± 0.21 GPa), followed by the mature HHL crosslink (39.9 ± 0.29 GPa), and then by the immature deH-HLNL and HLKNL crosslinks (37.9 ± 0.31 GPa and 37.7 ± 0.23 GPa, respectively). The strain energy vs. microfibril unit strain responses of the individual crosslinks revealed more pronounced differences, with PYD exhibiting the greatest stiffness, followed by HHL, and then by deH-HLNL and HLKNL. Bond dissociation energies were then used to predict potential sites of crosslink failure for the immature and mature crosslinks. Lastly, as a preliminary application, the uncrosslinked and crosslinked MD simulation data were used to predict the mechanical behavior of collagen fibrils exhibiting different levels of crosslinking; such an approach could also be extended to make predictions for fibrils with mixed crosslink compositions (e.g., X% uncrosslinked, Y% of immature HLKNL crosslink, and Z% of mature PYD crosslink). Thus, the work discussed herein can be helpful for the development of larger-scale models of crosslinked collagenous tissues

or materials (e.g., finite-element models [22] and mesoscopic models [30]).

Acknowledgements

We thank the Virginia Tech Department of Engineering Science and Mechanics and the Virginia Tech Advanced Research Computing unit for granting access to their high-performance computing resources. Graduate student support was received through the Harriett G. Jenkins Predoctoral Fellowship Project (National Aeronautics and Space Administration and the UNCF Special Programs Corporation) and the Virginia Tech-Initiative for Maximizing Student Development fellowship program (National Institutes of Health Biomedical and Behavioral Sciences Research Training Grant # R25 GM072767). This work was a part of a project funded by the National Science Foundation's Chemical, Bioengineering, Environmental, and Transport Systems Division (Award # 0932024 granted to R. De Vita, J. W. Freeman, and J. Barrett).

References

[1] K. Urich, Extracellular structural and secretory proteins, In: Comparative Animal Biochemistry, Springer-Verlag Berlin Heidelberg, New York, NY 1994, pp. 378–383.
[2] R.P. Boot-Handford, D.S. Tuckwell, Fibrillar collagen: The key to vertebrate evolution? A tale of molecular incest, BioEssays 25 (2003) 142–151, http://dx.doi.org/10.1002/bies.10230.
[3] A. Anasuya, B.S. Rao, Relationship between body collagen and urinary hydroxyproline excretion in young rats fed on a low-protein or low-calorie diet, Br. J. Nutr. 24 (1970) 97–107, http://dx.doi.org/10.1079/BJN19700013.
[4] M.L. Harkness, R.D. Harkness, D.W. James, The effect of a protein-free diet on the collagen content of mice, J. Physiol. 144 (1958) 307–313, http://dx.doi.org/10.1113/jphysiol.1958.sp006103.
[5] A.P. Williams, The amino acid, collagen and mineral composition of preruminant calves, J. Agric. Sci. 90 (1978) 617–624, http://dx.doi.org/10.1017/S0021859600056161.
[6] K. von der Mark, Structure, biosynthesis and gene regulation of collagens in cartilage and bone, in: M.J. Seibel, S.P. Robins, J.P. Bilezikian (Eds.), Dynamics of Bone and Cartilage Metabolism: Principles and Clinical Applications, second ed. Academic Press, Burlington, MA 2006, pp. 3–40.
[7] J. Brinckmann, Collagens at a glance, in: J. Brinckmann, H. Notbohm, P.K. Muller (Eds.), Collagen: Primer in Structure, Processing, and Assembly, Springer-Verlag Berlin Heidelberg, New York, NY 2005, pp. 1–6.
[8] S.M. Sweeney, J.P. Orgel, A. Fertala, J.D. McAuliffe, K.R. Turner, G.A. Di Lullo, et al., Candidate cell and matrix interaction domains on the collagen fibril, the predominant protein of vertebrates, J. Biol. Chem. 283 (2008) 21187–21197, http://dx.doi.org/10.1074/jbc.M709319200.
[9] N.C. Avery, A.J. Bailey, Restraining cross-links responsible for the mechanical properties of collagen fibers: Natural and artificial, in: P. Fratzl (Ed.), Collagen: Structure and Mechanics, Springer US, New York, NY 2008, pp. 81–91.
[10] D.R. Eyre, J.-J. Wu, Collagen cross-links, in: J. Brinckmann, H. Notbohm, P.K. Muller (Eds.), Collagen: Primer in Structure, Processing, and Assembly, Springer-Verlag Berlin Heidelberg, New York, NY 2005, pp. 207–229.
[11] D.R. Eyre, T.J. Koob, K.P. Van Ness, Quantitation of hydroxypyridinium crosslinks in collagen by high-performance liquid chromatography, Anal. Biochem. 137 (1984) 380–388, http://dx.doi.org/10.1016/0003-2697(84)90101-5.
[12] M. Saito, K. Marumo, Collagen cross-links as a determinant of bone quality: A possible explanation for bone fragility in aging, osteoporosis, and diabetes mellitus, Osteoporos. Int. 21 (2010) 195–214, http://dx.doi.org/10.1007/s00198-009-1066-z.
[13] D.R. Eyre, M.A. Paz, P.M. Gallop, Cross-linking in collagen and elastin, Annu. Rev. Biochem. 53 (1984) 717–748, http://dx.doi.org/10.1146/annurev.bi.53.070184.003441.
[14] M. Saito, K. Marumo, K. Fujii, N. Ishioka, Single-column high-performance liquid chromatographic fluorescence detection of immature, mature, and senescent cross-links of collagen, Anal. Biochem. 253 (1997) 26–32, http://dx.doi.org/10.1006/abio.1997.2350.
[15] O. Ishikawa, A. Kondo, Y. Miyachi, Mature type of skin collagen crosslink, histidinohydroxylysinonorleucine, is significantly increased in the skin of systemic sclerosis patients, Arthritis Rheum. 41 (1998) 376–377, http://dx.doi.org/10.1002/1529-0131(199802)41:2<376::AID-ART25>3.0.CO;2-J.
[16] A.J. van der Slot, A.M. Zuurmond, A.F. Bardoel, C. Wijmenga, H.E. Pruijs, D.O. Sillence, et al., Identification of PLOD2 as telopeptide lysyl hydroxylase, an important enzyme in fibrosis, J. Biol. Chem. 278 (2003) 40967–40972, http://dx.doi.org/10.1074/jbc.M307380200.
[17] Y.-L. Sun, Z.-P. Luo, A. Fertala, K.-N. An, Direct quantification of the flexibility of type I collagen monomer, Biochem. Biophys. Res. Commun. 295 (2002) 382–386, http://dx.doi.org/10.1016/S0006-291X(02)00685-X.
[18] Y.-L. Sun, Z.-P. Luo, A. Fertala, K.-N. An, Stretching type II collagen with optical tweezers, J. Biomech. 37 (2004) 1665–1669, http://dx.doi.org/10.1016/j.jbiomech.2004.02.028.
[19] L. Bozec, M. Horton, Topography and mechanical properties of single molecules of type I collagen using atomic force microscopy, Biophys. J. 88 (2005) 4223–4231, http://dx.doi.org/10.1529/biophysj.104.055228.
[20] A.C. Lorenzo, E.R. Caffarena, Elastic properties, Young's modulus determination and structural stability of the tropocollagen molecule: A computational study by steered molecular dynamics, J. Biomech. 38 (2005) 1527–1533, http://dx.doi.org/10.1016/j.jbiomech.2004.07.011.
[21] A. Gautieri, S. Vesentini, A. Redaelli, M.J. Buehler, Hierarchical structure and nanomechanics of collagen microfibrils from the atomistic scale up, Nano Lett. 11 (2011) 757–766, http://dx.doi.org/10.1021/nl103943u.
[22] R. Hambli, A. Barkaoui, Physically based 3D finite element model of a single mineralized collagen microfibril, J. Theor. Biol. 301 (2012) 28–41, http://dx.doi.org/10.1016/j.jtbi.2012.02.007.
[23] F. Hang, A.H. Barber, Nano-mechanical properties of individual mineralized collagen fibrils from bone tissue, J. R. Soc. Interface 8 (2011) 500–505, http://dx.doi.org/10.1098/rsif.2010.0413.
[24] J.A.J. van der Rijt, Micromechanical Testing of Single Collagen Type I Fibrils(Ph.D. Dissertation) University of Twente, 2004 (http://purl.utwente.nl/publications/41721).
[25] L. Yang, K.O. van der Werf, P.J. Dijkstra, J. Feijen, M.L. Bennink, Micromechanical analysis of native and cross-linked collagen type I fibrils supports the existence of microfibrils, J. Mech. Behav. Biomed. Mater. 6 (2012) 148–158, http://dx.doi.org/10.1016/j.jmbbm.2011.11.008.
[26] Z.L. Shen, M.R. Dodge, H. Kahn, R. Ballarini, S.J. Eppell, Stress-strain experiments on individual collagen fibrils, Biophys. J. 95 (2008) 3956–3963, http://dx.doi.org/10.1529/biophysj.107.124602.
[27] Z.L. Shen, M.R. Dodge, H. Kahn, R. Ballarini, S.J. Eppell, In vitro fracture testing of submicron diameter collagen fibril specimens, Biophys. J. 99 (2010) 1986–1995, http://dx.doi.org/10.1016/j.bpj.2010.07.021.
[28] S.J. Eppell, B.N. Smith, H. Kahn, R. Ballarini, Nano measurements with micro-devices: Mechanical properties of hydrated collagen fibrils, J. R. Soc. Interface 3 (2006) 117–121, http://dx.doi.org/10.1098/rsif.2005.0100.
[29] A. Gautieri, S. Vesentini, A. Redaelli, M.J. Buehler, Viscoelastic properties of model segments of collagen molecules, Matrix Biol. 31 (2012) 141–149, http://dx.doi.org/10.1016/j.matbio.2011.11.005.
[30] M.J. Buehler, Nanomechanics of collagen fibrils under varying cross-link densities: Atomistic and continuum studies, J. Mech. Behav. Biomed. Mater. 1 (2008) 59–67, http://dx.doi.org/10.1016/j.jmbbm.2007.04.001.
[31] Discovery studio modeling environment, version 3.1, Accelrys Software, Inc., San Diego, CA, 2011.
[32] W. Humphrey, A. Dalke, K. Schulten, VMD: Visual molecular dynamics, J. Mol. Graph. 14 (1996) 33–38, http://dx.doi.org/10.1016/0263-7855(96)00018-5.
[33] J.C. Phillips, R. Braun, W. Wang, J. Gumbart, E. Tajkhorshid, E. Villa, et al., Scalable molecular dynamics with NAMD, J. Comput. Chem. 26 (2005) 1781–1802, http://dx.doi.org/10.1002/jcc.20289.
[34] J.E. Stone, An Efficient Library for Parallel Ray Tracing and Animation(M.S. Thesis) University of Missouri-Rolla, 1998 (http://hdl.handle.net/10355/22017).
[35] F.A. Momany, R. Rone, Validation of the general purpose QUANTA ®3.2/CHARMm® force field, J. Comput. Chem. 13 (1992) 888–900, http://dx.doi.org/10.1002/jcc.540130714.
[36] R. Berisio, L. Vitagliano, L. Mazzarella, A. Zagari, Crystal structure of the collagen triple helix model [(Pro-Pro-Gly)(10)](3), Protein Sci. 11 (2002) 262–270, http://dx.doi.org/10.1110/ps.32602.
[37] J.M. Chen, C.E. Kung, S.H. Feairheller, E.M. Brown, An energetic evaluation of a "Smith" collagen microfibril model, J. Protein Chem. 10 (1991) 535–552, http://dx.doi.org/10.1007/BF01025482.
[38] R.D. Fraser, T.P. MacRae, A. Miller, E. Suzuki, Molecular conformation and packing in collagen fibrils, J. Mol. Biol. 167 (1983) 497–521, http://dx.doi.org/10.1016/S0022-2836(83)80347-7.
[39] T.J. Wess, A.P. Hammersley, L. Wess, A. Miller, A consensus model for molecular packing of type I collagen, J. Struct. Biol. 122 (1998) 92–100, http://dx.doi.org/10.1006/jsbi.1998.3991.
[40] J.P.R.O. Orgel, A. Miller, T.C. Irving, R.F. Fischetti, A.P. Hammersley, T.J. Wess, The in situ supermolecular structure of type I collagen, Structure 9 (2001) 1061–1069, http://dx.doi.org/10.1016/S0969-2126(01)00669-4.
[41] J.P.R.O. Orgel, T.C. Irving, A. Miller, T.J. Wess, Microfibrillar structure of type I collagen in situ, Proc. Natl. Acad. Sci. U. S. A. 103 (2006) 9001–9005, http://dx.doi.org/10.1073/pnas.0502718103.
[42] D.A. Hanson, D.R. Eyre, Molecular site specificity of pyridinoline and pyrrole cross-links in type I collagen of human bone, J. Biol. Chem. 271 (1996) 26508–26516, http://dx.doi.org/10.1074/jbc.271.43.26508.
[43] G.L. Mechanic, E.P. Katz, M. Henmi, C. Noyes, M. Yamauchi, Locus of a histidine-based, stable trifunctional, helix to helix collagen cross-link: Stereospecific collagen structure of type I skin fibrils, Biochemistry 26 (1987) 3500–3509, http://dx.doi.org/10.1021/bi00386a038.
[44] M. Yamauchi, R.E. London, C. Guenat, F. Hashimoto, G.L. Mechanic, Structure and formation of a stable histidine-based trifunctional cross-link in skin collagen, J. Biol. Chem. 262 (1987) 11428–11434, http://www.jbc.org/content/262/24/11428.abstract.
[45] P.P. Fietzek, K. Kuhn, The primary structure of collagen, in: D.A. Hall, D.S. Jackson (Eds.), International Review of Connective Tissue Research, 7, Academic Press, New York, NY 1976, pp. 1–60.
[46] The UniProt Consortium, Reorganizing the protein space at the Universal Protein Resource (UniProt), Nucleic Acids Res. 40 (2012) D71–D75, http://dx.doi.org/10.1093/nar/gkr981.
[47] A. Onufriev, D. Bashford, D.A. Case, Modification of the generalized Born model suitable for macromolecules, J. Phys. Chem. B 104 (2000) 3712–3720, http://dx.doi.org/10.1021/jp994072s.
[48] M. Bhandarkar, A. Bhatele, E. Bohm, R. Brunner, F. Buelens, C. Chipot, et al., NAMD user's guide, Version 2.8, 2011 (http://www.ks.uiuc.edu/Research/namd/2.8/ug/).

[49] A.L. Kwansa, R. De Vita, J.W. Freeman, Mechanical recruitment of N- and C-crosslinks in collagen type I, Matrix Biol. 34 (2014) 161–169, http://dx.doi.org/10.1016/j.matbio.2013.10.012.
[50] C.S. Chiang, A. Anishkin, S. Sukharev, Gating of the large mechanosensitive channel in situ: Estimation of the spatial scale of the transition from channel population responses, Biophys. J. 86 (2004) 2846–2861, http://dx.doi.org/10.1016/S0006-3495(04)74337-4.
[51] MATLAB, version R2012b, The MathWorks, Inc., Natick, MA, 1984.
[52] JMP, version 9.0, SAS Institute, Inc., Cary, NC, 2010.
[53] Y.P. Kato, D.L. Christiansen, R.A. Hahn, S.-J. Shieh, J.D. Goldstein, F.H. Silver, Mechanical properties of collagen fibres: A comparison of reconstituted and rat tail tendon fibres, Biomaterials 10 (1989) 38–42, http://dx.doi.org/10.1016/0142-9612(89)90007-0.
[54] J.A.J. van der Rijt, K.O. van der Werf, M.L. Bennink, P.J. Dijkstra, J. Feijen, Micromechanical testing of individual collagen fibrils, Macromol. Biosci. 6 (2006) 697–702, http://dx.doi.org/10.1002/mabi.200600063.
[55] H. Lu, B. Isralewitz, A. Krammer, V. Vogel, K. Schulten, Unfolding of titin immunoglobulin domains by steered molecular dynamics simulation, Biophys. J. 75 (1998) 662–671, http://dx.doi.org/10.1016/S0006-3495(98)77556-3.
[56] M. Gao, D. Craig, O. Lequin, I.D. Campbell, V. Vogel, K. Schulten, Structure and functional significance of mechanically unfolded fibronectin type III1 intermediates, Proc. Natl. Acad. Sci. 100 (2003) 14784–14789, http://dx.doi.org/10.1073/pnas.2334390100.
[57] A. Gautieri, M.J. Buehler, A. Redaelli, Deformation rate controls elasticity and unfolding pathway of single tropocollagen molecules, J. Mech. Behav. Biomed. 2 (2009) 130–137, http://dx.doi.org/10.1016/j.jmbbm.2008.03.001.
[58] A. Masic, L. Bertinetti, R. Schuetz, S.-W. Chang, T.H. Metzger, M.J. Buehler, et al., Osmotic pressure induced tensile forces in tendon collagen, Nat. Commun. 6 (1–8) (2015) 5942, http://dx.doi.org/10.1038/ncomms6942.
[59] J. Bella, B. Brodsky, H.M. Berman, Hydration structure of a collagen peptide, Structure 3 (1995) 893–906, http://dx.doi.org/10.1016/S0969-2126(01)00224-6.
[60] A.D. MacKerell, D. Bashford, M. Bellott, R.L. Dunbrack, J.D. Evanseck, M.J. Field, et al., All-atom empirical potential for molecular modeling and dynamics studies of proteins, J. Phys. Chem. B 102 (1998) 3586–3616, http://dx.doi.org/10.1021/jp973084f.
[61] F. Jensen, Force field methods, Introduction to Computational Chemistry, second ed. Wiley, West Sussex, England 2007, pp. 25–27,63.
[62] P. Morse, Diatomic molecules according to the wave mechanics. II. Vibrational levels, Phys. Rev. 34 (1929) 57–64, http://dx.doi.org/10.1103/PhysRev.34.57.
[63] J.A. Dean, Properties of atoms, radicals, and bonds, in: Lange's Handbook of Chemistry, 15th ed. McGraw-Hill, New York, NY 1999, pp. 4.41–4.53.
[64] M. Yamauchi, Collagen: The major matrix molecule in mineralized tissues, in: J.J.B. Anderson, S.C. Garner (Eds.), Calcium and Phosphorus in Health and Disease, CRC Press, Boca Raton, FL 1996, pp. 134–137.
[65] S.P. Robins, A. Duncan, Cross-linking of collagen. Location of pyridinoline in bovine articular cartilage at two sites of the molecule, Biochem. J. 215 (1983) 175–182, http://dx.doi.org/10.1042/bj2150175.
[66] R. Kuypers, M. Tyler, L.B. Kurth, I.D. Jenkins, D.J. Horgan, Identification of the loci of the collagen-associated Ehrlich chromogen in type I collagen confirms its role as a trivalent cross-link, Biochem. J. 283 (Pt 1) (1992) 129–136, http://dx.doi.org/10.1042/bj2830129.
[67] M. Yamauchi, G.S. Chandler, H. Tanzawa, E.P. Katz, Cross-linking and the molecular packing of corneal collagen, Biochem. Biophys. Res. Commun. 219 (1996) 311–315, http://dx.doi.org/10.1006/bbrc.1996.0229.
[68] K. Fujii, T. Yamagishi, T. Nagafuchi, M. Tsuji, Y. Kuboki, Biochemical properties of collagen from ligaments and periarticular tendons of the human knee, Knee Surg. Sports Traumatol. Arthrosc. 2 (1994) 229–233, http://dx.doi.org/10.1007/BF01845593.
[69] D. Amiel, J.B. Kleiner, Biochemistry of tendon and ligament, in: M.E. Nimni (Ed.), Collagen: Biotechnology, CRC Press, Boca Raton, FL 1988, pp. 223–251.
[70] K. Marumo, M. Saito, T. Yamagishi, K. Fujii, The "ligamentization" process in human anterior cruciate ligament reconstruction with autogenous patellar and hamstring tendons: A biochemical study, Am. J. Sports Med. 33 (2005) 1166–1173, http://dx.doi.org/10.1177/0363546504271973.
[71] T.J. Sims, A.J. Bailey, Quantitative analysis of collagen and elastin cross-links using a single-column system, J. Chromatogr. 582 (1992) 49–55, http://dx.doi.org/10.1016/0378-4347(92)80301-6.
[72] A.L. Kwansa, Molecular Dynamics and Mechanical Behavior of Collagen Type I and its Lysine/Hydroxylysine-Derived Crosslinks(Ph.D. Dissertation) Virginia Polytechnic Institute and State University, 2013 (http://hdl.handle.net/10919/50933).
[73] R.B. Svensson, T. Hassenkam, P. Hansen, S. Peter Magnusson, Viscoelastic behavior of discrete human collagen fibrils, J. Mech. Behav. Biomed. Mater. 3 (2010) 112–115, http://dx.doi.org/10.1016/j.jmbbm.2009.01.005.
[74] ACD/ChemSketch Freeware, version 11.0, Advanced Chemistry Development, Inc., Toronto, ON, Canada, 2007 (www.acdlabs.com).
[75] A.J. Bailey, R.G. Paul, L. Knott, Mechanisms of maturation and ageing of collagen, Mech. Ageing Dev. 106 (1998) 1–56, http://dx.doi.org/10.1016/S0047-6374(98)00119-5.
[76] M. Tarini, P. Cignoni, C. Montani, Ambient occlusion and Edge cueing for enhancing real time molecular visualization, IEEE Trans. Vis. Comput. Graph. 12 (2006) 1237–1244, http://dx.doi.org/10.1109/TVCG.2006.115.